Successful Kinetic Impact into an Asteroid for Planetary Defense

R. Terik Daly*†[1]
Carolyn M. Ernst*[1]
Olivier S. Barnouin*[1]
Nancy L. Chabot[1]
Andrew S. Rivkin[1]
Andrew F. Cheng[1]
Elena Y. Adams[1]
Harrison F. Agrusa[2]
Elisabeth D. Abel[1]
Amy L. Alford[1]
Erik I. Asphaug[3]
Justin A. Atchison[1]
Andrew R. Badger[1]
Paul Baki[4]
Ronald-L. Ballouz[1]
Dmitriy L. Bekker[1]
Julie Bellerose[5]
Shyam Bhaskaran[5]
Bonnie J. Buratti[5]
Saverio Cambioni[6]
Michelle H. Chen[1]
Steven R. Chesley[5]
George Chiu[1]
Gareth S. Collins[7]
Matthew W. Cox[1]
Mallory E. DeCoster[1]
Peter S. Ericksen[1]
Raymond C. Espiritu[1]
Alan S. Faber[1]
Tony L. Farnham[2]
Fabio Ferrari[8]
Zachary J. Fletcher[1]
Robert W. Gaskell[9]
Dawn M. Graninger[1]
Musad A. Haque[1]
Patricia A. Harrington-Duff[1]
Sarah Hefter[1]
Isabel Herreros[10]
Masatoshi Hirabayashi[11]
Philip M. Huang[1]
Syau-Yun W. Hsieh[1]
Seth A. Jacobson[12]
Stephen N. Jenkins[1]
Mark A. Jensenius[1]
Jeremy W. John[1]
Martin Jutzi[13]
Tomas Kohout[14,15]
Timothy O. Krueger[1]
Frank E. Laipert[5‡]
Norberto R. Lopez[1]
Robert Luther[16]
Alice Lucchetti[17]
Declan M. Mages[5]
Simone Marchi[18]
Anna C. Martin[1]
Maria E. McQuaide[1]
Patrick Michel[19]
Nicholas A. Moskovitz[20]
Ian W. Murphy[1]
Naomi Murdoch[21]
Shantanu P. Naidu[5]
Hari Nair[1]
Michael C. Nolan[3]
Jens Ormö[10]
Maurizio Pajola[17]
Eric E. Palmer[9]
James M. Peachey[1]
Petr Pravec[22]
Sabina D. Raducan[13]
K.T. Ramesh[23]
Joshua R. Ramirez[1]
Edward L. Reynolds[1]
Joshua E. Richman[1]
Colas Q. Robin[21]
Luis M. Rodriguez[1]
Lew M. Roufberg[1]
Brian P. Rush[5]
Carolyn A. Sawyer[1]
Daniel J. Scheeres[24]
Petr Scheirich[22]
Stephen R. Schwartz[9]
Matthew P. Shannon[1]
Brett N. Shapiro[1]
Caitlin E. Shearer[1]
Evan J. Smith[1]
R. Joshua Steele[1]
Jordan K Steckloff[9]
Angela M. Stickle[1]
Jessica M. Sunshine[2]
Emil A. Superfin[1]
Zahi B. Tarzi[5]
Cristina A. Thomas[25]
Justin R. Thomas[1]
Josep M. Trigo-Rodríguez[26]
B. Teresa Tropf[1]
Andrew T. Vaughan[5]
Dianna Velez[5]
C. Dany Waller[1]
Daniel S. Wilson[1]
Kristin A. Wortman[1]
Yun Zhang[2]

[1]Johns Hopkins University Applied Physics Laboratory, Laurel, MD, USA

[2]University of Maryland, College Park, MD, USA

[3]University of Arizona, Tucson, AZ, USA

[4]Technical University of Kenya, Nairobi, Kenya

[5]Jet Propulsion Laboratory, California Institute of Technology, Pasadena, CA, USA

[6]Massachusetts Institute of Technology, Cambridge, MA, USA

[7]Imperial College, London, UK

[8]Politecnico di Milano, Milano, Italy

[9]Planetary Science Institute, Tucson, AZ, USA

[10]Centro de Astrobiologiá (CAB) CSIC-INTA, Carretera de Ajalvir km4, 28850 Torrejón de Ardoz, Spain

[11]Auburn University, Auburn, AL, USA

[12]Michigan State University, East Lansing, MI, USA

[13]University of Bern, Bern, Switzerland

[14]Institute of Geology of the Czech Academy of Sciences, Prague, Czech Republic

[15]University of Helsinki, Helsinki Finland

[16]Museum für Naturkunde, Leibniz Institute for Evolution and Biodiversity Science, Berlin, Germany

[17]INAF-Astronomical Observatory of Padova, Padova, Italy

[18]Southwest Research Institute, Boulder, CO, USA

[19]Université Côte d'Azur, Observatoire de la Côte d'Azur, CNRS, Laboratoire Lagrange, Nice, France

[20]Lowell Observatory, Flagstaff, AZ, USA

[21]ISAE-SUPAERO, Université de Toulouse, Toulouse, France

[22]Astronomical Institute AS CR, Ondrejov, Czech Republic

[23]Johns Hopkins University, Baltimore, MD, USA

[24]University of Colorado, Boulder, CO, USA

[25]Northern Arizona University, Flagstaff, AZ, USA

[26]Institute of Space Sciences, Barcelona, Spain

*These authors contributed equally to this work.

[†]Corresponding author

[‡]Currently at Nabla Zero Labs, South Pasadena, CA, USA

While no known asteroid poses a threat to Earth for at least the next century, the catalog of near-Earth asteroids is incomplete for objects whose impacts would produce regional devastation[1,2]. Several approaches have been proposed to potentially prevent an asteroid impact with Earth by deflecting or disrupting an asteroid[1–3]. A test of kinetic impact technology *was identified as the highest priority space mission related to asteroid* mitigation[1]. *NASA's Double Asteroid Redirection Test (DART) mission is the first full-scale test of kinetic impact technology. The mission's target asteroid was Dimorphos, the secondary member of the S-type binary near-Earth asteroid (65803) Didymos. This binary asteroid system was chosen to enable ground-based telescopes to quantify the asteroid deflection caused by DART's impact*[4]. While past missions have utilized impactors to investigate the properties of small bodies[5,6], those earlier missions were not intended to deflect their targets and did not achieve measurable deflections. Here we report the DART spacecraft's autonomous kinetic impact into Dimorphos and reconstruct the impact event, including the timeline leading to impact, the location and nature of the DART impact site, and the size and shape of Dimorphos. The successful impact of the DART spacecraft with Dimorphos and the resulting change in Dimorphos's orbit[7] demonstrates that kinetic impactor technology is a viable technique to potentially defend Earth if necessary.

The DART spacecraft launched on 24 November 2021. The spacecraft carried a narrow-angle imager called the Didymos Reconnaissance and Asteroid Camera for Optical navigation (DRACO), which was used for optical navigation, terminal guidance, and asteroid characterization[8]. DRACO detected Didymos—the primary asteroid in the binary system—in summed optical navigation images 61 days before impact. On 27 August 2022, 30 days before impact, DRACO began taking optical navigation images of Didymos every five hours, which were processed by the ground optical navigation team[9].

On 26 September 2022 at 19:09:24 UTC, four hours and five minutes before impact, the spacecraft's autonomous Small-body Maneuvering Autonomous Real Time Navigation (SMART Nav) system[10] took control of spacecraft navigation (Figure 1a). SMART Nav processed DRACO images onboard[11] to identify Didymos, and once resolved, Dimorphos. To achieve impact with Dimorphos, the spacecraft needed to distinguish between the two asteroids and hit the smaller, dimmer one. Due to the dynamics of the binary system and the spatial resolution of DRACO, it was known that the spacecraft's ultimate target—Dimorphos–would be hidden from DRACO's view during most of the autonomous phase. By design, SMART Nav maneuvered the spacecraft towards Didymos until Dimorphos became reliably detected[10]. SMART Nav first detected Dimorphos 73 minutes prior to impact, and at 50 minutes prior to impact, SMART Nav began maneuvering towards Dimorphos (Figure 1). As planned, SMART Nav maneuvering ended at 23:11:52 UTC, 2.5 minutes before impact, to give the spacecraft time to settle to minimize jitter and smear in final images. The spacecraft impacted Dimorphos at 23:14:24.183 ± 0.004 UTC (see methods). From the start of autonomous navigation until impact, the spacecraft continuously streamed images to the ground, which were immediately broadcast to the public.

*The final full image was acquired 1.818 seconds before impact and has a pixel scale of 5.5 cm. The final image received on the ground was a partial image acquired 0.85***5*** seconds before impact with a pixel scale of 2.6 cm.*

Little was known about the shape or surface of Dimorphos until DRACO obtained high-resolution images. Ground-based radar observations[12] led to a diameter estimate of 150±30 m. Analysis of telescopic photometric observations yielded a comparable diameter for Dimorphos, 171±11 m[13,14]. Although DRACO imaged only a portion of Dimorphos, and illumination was limited at 60° solar phase, the images were used to construct an asteroid shape model (see methods). The shape model revealed Dimorphos to be an oblate spheroid with a volume-equivalent diameter of 151± 5 m (Table 1; Figure 2; Extended Data Fig. 1). Dimorphos's shape is unusual relative to other near-Earth asteroids visited by spacecraft[15–19] and differs from other binary asteroid secondaries observed to date that have measured elongations[20–23]. However, oblate secondaries show little or no measurable lightcurve amplitude, which biases the observational sample toward elongated secondaries. A new size estimate for Didymos from DRACO images (Table 1) (see methods) combined with previous telescopic observations[4] enables calculation of a more accurate visible (0.55 μm) geometric albedo for the system of 0.15 ± 0.02. This value is on the low side, but within one sigma, of the mean geometric albedo for S-type asteroids[24].

The spacecraft trajectory and pointing were reconstructed to locate the impact site (see methods) (Figure 2). The spacecraft impacted Dimorphos at 8.84 ± 0.45º S, 264.30 ± 0.47º E, within 25 m of the center of the figure, which is very near the scenario for maximizing momentum transfer

with an impact through the center of figure[25]. The one-sigma uncertainty in the impact site location is ± 68 cm (see methods), which is smaller than the size of the spacecraft bus (Figure 3). The impact angle was 73 ± 7º degrees from local horizontal (see methods and Extended Data Fig. 2). The impact site was near two large boulders, labeled boulder 1 (6.5-m long and at its highest point standing ~2.2 m above the surrounding terrain; see Extended Data Figure 3) and boulder 2 (6.1-m long and at its highest point standing ~1.6 m above the surrounding terrain; see Extended Data Figure 3) in Figure 2b and 2c. The spacecraft approached the asteroid with its solar arrays canted slightly toward the surface (Figure 3). The leading edge of the +Y solar array contacted the surface of boulder 1, and this solar array directly hit boulder 1 (Figure 3). Almost immediately thereafter, the -Y solar array grazed boulder 2, with the leading edge of the -Y array contacting the surface near the base of boulder 2 in downrange direction (Figure 3). Finally, the spacecraft bus hit between boulders 1 and 2 (Figure 3). Although the solar arrays contacted Dimorphos just prior to the spacecraft bus, the bulk of the spacecraft's energy was transferred by the bus, which accounted for ~88% of the spacecraft mass at the time of impact.

DART images of Dimorphos revealed a boulder-strewn surface (Figure 2a, Extended Data Figs. 4 and 5) resembling other small NEAs, such as the S-type (25143) Itokawa[17], and carbonaceous asteroids (101955) Bennu[26], and (162173) Ryugu[16], suggesting a rubble-pile structure for Dimorphos. The boulder-rich nature of the surface is apparent in images as coarse as 2–3 m pixel scale (Extended Data Fig. 4). No unambiguous impact crater candidates are observed, which indicates a young surface, though craters can be difficult to identify on boulder-covered terrains[27–30]. The appearance of Dimorphos contrasts with impressions from lower-resolution

images of the Didymos surface, where regional roughness variations are apparent (Extended Data Fig. 4).

The final complete DRACO image captured a ~880 m^2 area surrounding the impact site at a 5.5-cm pixel scale. The impact region (Figure 2b) exhibits blocky terrain resembling the rest of the observed hemisphere (Figure 2a; Extended Data Fig. 4 and 5). There is evidence for variation within boulders, “rocks on rocks” similar to observations on Bennu[31], and partially buried boulders (Extended Data Fig. 5). The longest axes of boulders counted in the final complete image are 0.16 m to 6.5 m in length. The impact region has fewer boulders in the 0.2–0.5 m size range than expected if the cumulative distribution followed a single power-law, even though the pixel scale of the image is sufficient for their identification (Extended Data Fig. 6). There is no evidence for expansive smooth deposits (grain size smaller than the image pixel scale) such as those seen on Itokawa[17]. The blocky nature of the impact site likely influenced crater formation, ejecta, and momentum enhancement, as seen in impact experiments[28,32–34], numerical simulations[25,35], and the Small Carry-on Impactor experiment on Hayabusa2[5].

Table 1. Properties of the DART impact, Dimorphos, and Didymos.

Time of impact	26 September 2022 at 23:14:24.183 ± 0.004 UTC
Impact speed (km/s)	6.1449 ± 0.0003
Impact angle (degrees)	73 ± 7 from local horizontal, 17 ± 7 from the surface normal
Impact site location (latitude, longitude	8.84 ± 0.45° S, 264.30 ± 0.47° E
Impact site offset from center of figure (m)	25 ± 1
Spacecraft mass at time of impact (kg)	579.4 ± 0.7
Impact kinetic energy (GJ)	10.94 ± 0.01
Extent of Dimorphos (m)	X: 177 ± 2 Y: 174 ± 4 Z: 116 ± 2
Extent of Didymos (m)	X: 849 ± 15 Y: 851 ± 15 Z: 620 ± 15
Volume of Dimorphos (km^3)	0.00181 ± 10%
Diameter of volume-equivalent sphere for Dimorphos (m)*	151 ± 5
Diameter of volume-equivalent sphere for Didymos (m)*	761 ± 26
Mass of the Didymos system (kg)	$(5.6 \pm 0.5) \times 10^{11}$
Density of Didymos system (kg/m^3)	2400 ± 300
Inferred Mass of Dimorphos (kg)	4.3×10^9

*Computed from the volumes of the shape models, not the volumes of triaxial ellipsoids with the extents listed above.

DART did not measure the mass of Dimorphos. Instead, Dimorphos's mass is estimated using the orbital properties of the binary system, the total volume of the system, and an assumption that Didymos and Dimorphos have equal bulk densities (see methods). This assumption cannot be rigorously tested from DART data, but this approach leads to a bulk density of Dimorphos of 2400 kg/m^3 (Table 1) with difficult-to-quantify uncertainties.

Based on analyses of reflectance spectra, the best meteoritic analogs for Didymos are L and LL chondrites[36,37]. L and LL chondrites have grain densities[38] of 3580 ± 10 kg/m^3 and 3520 ± 10 kg/m^3, respectively. If one assumes Dimorphos has the same composition as Didymos and that these meteorite values represent the grain density of Dimorphos, then a bulk density of ~2400 kg/m^3 implies a Dimorphos bulk porosity of order 30% (with a difficult-to-quantify uncertainty; see methods). This level of bulk porosity is not inconsistent with a rubble-pile structure for Dimorphos, a structure suggested by the boulder-rich character of Dimorphos's surface. This bulk porosity likely exists as a combination of macroporosity between pieces of rubble and microporosity within individual pieces of rubble. L and LL chondrite samples have porosities of 8.0 ± 0.3% and 9.5 ± 0.6%, respectively[38], which would imply that macroporosity is substantial on Dimorphos. Estimates of the density and porosity of Dimorphos will be significantly improved when ESA's Hera mission arrives at the Didymos system in early 2027[39].

DART's successful autonomous targeting of a small asteroid with limited prior knowledge is a key first accomplishment on the path to advancing kinetic impactor technology to an operational capability. DART's impact indicates that a precursor reconnaissance mission is not a prerequisite for intercepting a sub-kilometer asteroid, though the characterization done by a precursor

mission would provide valuable information for optimizing, planning and predicting the outcome with greater certainty. Kinetic impactor technology for asteroid deflection requires having sufficient warning time–at least several years but preferably decades–to prevent an asteroid impact with the Earth[1–3]. Nevertheless, this first successful step to demonstrate the viability of kinetic impactor technology for planetary defense builds optimism about humanity's capacity to protect the Earth from an asteroid threat.

References

1. *Defending Planet Earth: Near-Earth Object Surveys and Hazard Mitigation Strategies*. 12842 (National Academies Press, 2010). doi:10.17226/12842.
2. Interagency Working Group for Detecting and Mitigating the Impact of Earth-bound Near-Earth Objects. National Near-Earth Object Preparedness Strategy and Action Plan. (2018).
3. Committee on the Planetary Science and Astrobiology Decadal Survey, Space Studies Board, Division on Engineering and Physical Sciences, & National Academies of Sciences, Engineering, and Medicine. *Origins, Worlds, and Life: A Decadal Strategy for Planetary Science and Astrobiology 2023-2032*. 26522 (National Academies Press, 2022). doi:10.17226/26522.
4. *Rivkin, A. S. et al. The Double Asteroid Redirection Test (DART): Planetary Defense Investigations and Requirements.* Planet. Sci. J. ***2**, 173 (2021).*
5. A'Hearn, M. F. *et al.* Deep impact: excavating comet Tempel 1. *science* **310**, 258–264 (2005).
6. Arakawa, M. *et al.* An artificial impact on the asteroid (162173) Ryugu formed a crater in the gravity-dominated regime. *Science* **368**, 67–71 (2020).

7. Thomas, C. A. Orbital Period Change of Dimorphos Due to the DART Kinetic Impact. *Nature* **(this issue)**, (2022).
8. Fletcher, Z. J. *et al.* Didymos Reconnaissance and Asteroid Camera for OpNav (DRACO): design, fabrication, test, and operation. in *Space Telescopes and Instrumentation 2022: Optical, Infrared, and Millimeter Wave* (eds. Coyle, L. E., Perrin, M. D. & Matsuura, S.) 11 (SPIE, 2022). doi:10.1117/12.2627873.
9. Rush, B. P. *et al.* Optical Navigation for the DART Mission. in *33rd AAS/AIAA Space Flight Mechanics Meeting*, Austin TX, 15 19, January 2023 (AAS 23-234).
10. Adams, E. *et al.* Double Asteroid Redirection Test: The Earth Strikes Back. in *2019 IEEE Aerospace Conference* 1–11 (IEEE, 2019). doi:10.1109/AERO.2019.8742007.
11. Bekker, D., Smith, R. & Tran, M. Q. Guiding DART to Impact — the FPGA SoC Design of the DRACO Image Processing Pipeline. in *2021 IEEE Space Computing Conference (SCC)* 122–133 (IEEE, 2021). doi:10.1109/SCC49971.2021.00020.
12. Naidu, S. P. *et al.* Radar observations and a physical model of binary near-Earth asteroid 65803 Didymos, target of the DART mission. *Icarus* **348**, 113777 (2020).
13. Pravec, P. *et al.* Photometric Observations of the Binary Near-Earth Asteroid (65803) Didymos in 2015–2021 Prior to DART Impact. *Planet. Sci. J.* **3**, 175 (2022).
14. Scheirich, P. & Pravec, P. Preimpact Mutual Orbit of the DART Target Binary Asteroid (65803) Didymos Derived from Observations of Mutual Events in 2003–2021. *Planet. Sci. J.* **3**, 163 (2022).
15. Zuber, M. T. *et al.* The Shape of 433 Eros from the NEAR-Shoemaker Laser Rangefinder. *Science* **289**, 2097–2101 (2000).

16. Watanabe, S. *et al.* Hayabusa2 arrives at the carbonaceous asteroid 162173 Ryugu—A spinning top–shaped rubble pile. *Science* **364**, 268–272 (2019).

17. Fujiwara, A. *et al.* The Rubble-Pile Asteroid Itokawa as Observed by Hayabusa. *Science* **312**, 1330–1334 (2006).

18. Huang, J. *et al.* The Ginger-shaped Asteroid 4179 Toutatis: New Observations from a Successful Flyby of Chang'e-2. *Sci. Rep.* **3**, 3411 (2013).

19. Barnouin, O. S. *et al.* Shape of (101955) Bennu indicative of a rubble pile with internal stiffness. *Nat. Geosci.* **12**, 247–252 (2019).

20. Ostro, Steven. J. *et al.* Radar Imaging of Binary Near-Earth Asteroid (66391) 1999 KW4. *Science* **314**, 1276–1280 (2006).

21. Becker, T. M. *et al.* Physical modeling of triple near-Earth Asteroid (153591) 2001 SN263 from radar and optical light curve observations. *Icarus* **248**, 499–515 (2015).

22. Naidu, S. P. *et al.* RADAR IMAGING AND CHARACTERIZATION OF THE BINARY NEAR-EARTH ASTEROID (185851) 2000 DP107. *Astron. J.* **150**, 54 (2015).

23. Pravec, P. *et al.* Binary asteroid population. 3. Secondary rotations and elongations. *Icarus* **267**, 267–295 (2016).

24. Pravec, P., Harris, A. W., Kušnirák, P., Galád, A. & Hornoch, K. Absolute magnitudes of asteroids and a revision of asteroid albedo estimates from WISE thermal observations. *Icarus* **221**, 365–387 (2012).

25. Stickle, A. M. *et al.* Effects of Impact and Target Parameters on the Results of a Kinetic Impactor: Predictions for the Double Asteroid Redirection Test (DART) Mission. *Planet. Sci. J.* **3**, 248 (2022).

26. Lauretta, D. S. *et al.* The unexpected surface of asteroid (101955) Bennu. *Nature* **568**, 55–60 (2019).

27. Hirata, N. *et al.* A survey of possible impact structures on 25143 Itokawa. *Icarus* **200**, 486–502 (2009).

28. Barnouin, O. S., Daly, R. T., Cintala, M. J. & Crawford, D. A. Impacts into coarse-grained spheres at moderate impact velocities: Implications for cratering on asteroids and planets. *Icarus* **325**, 67–83 (2019).

29. Hirata, N. *et al.* The spatial distribution of impact craters on Ryugu. *Icarus* **338**, 113527 (2020).

30. Daly, R. T. *et al.* The Morphometry of Impact Craters on Bennu. *Geophys. Res. Lett.* **47**, (2020).

31. Jawin, E. R. *et al.* Global Patterns of Recent Mass Movement on Asteroid (101955) Bennu. *J. Geophys. Res. Planets* **125**, (2020).

32. Tatsumi, E. & Sugita, S. Cratering efficiency on coarse-grain targets: Implications for the dynamical evolution of asteroid 25143 Itokawa. *Icarus* **300**, 227–248 (2018).

33. Okawa, H. *et al.* Effect of boulder size on ejecta velocity scaling law for cratering and its implication for formation of tiny asteroids. *Icarus* **387**, 115212 (2022).

34. Ormö, J. *et al.* Boulder exhumation and segregation by impacts on rubble-pile asteroids. *Earth Planet. Sci. Lett.* **594**, 117713 (2022).

35. Raducan, S. D., Jutzi, M., Zhang, Y., Ormö, J. & Michel, P. Reshaping and ejection processes on rubble-pile asteroids from impacts. *Astron. Astrophys.* **665**, L10 (2022).

36. de León, J., Licandro, J., Duffard, R. & Serra-Ricart, M. Spectral analysis and mineralogical characterization of 11 olivine–pyroxene rich NEAs. *Adv. Space Res.* **37**, 178–183 (2006).

37. Dunn, T. L., Burbine, T. H., Bottke, W. F. & Clark, J. P. Mineralogies and source regions of near-Earth asteroids. *Icarus* **222**, 273–282 (2013).

38. Flynn, G. J., Consolmagno, G. J., Brown, P. & Macke, R. J. Physical properties of the stone meteorites: Implications for the properties of their parent bodies. *Geochemistry* **78**, 269–298 (2018).

39. Michel, P. *et al.* The ESA Hera Mission: Detailed Characterization of the DART Impact Outcome and of the Binary Asteroid (65803) Didymos. *Planet. Sci. J.* **3**, 160 (2022).

Figure Captions

Figure 1. Milestones leading to impact with Dimorphos from the time SMART Nav began targeting until the end of SMART Nav maneuvering. Each column corresponds to a milestone. Each row shows, from top to bottom, the raw DRACO image at the time of that milestone with circles indicating the two asteroids detected by onboard processing and identified by SMART Nav (yellow dashed circles, Didymos; green solid circles, Dimorphos), a zoom-in of Didymos, and a zoom-in of Dimorphos. The SMART Nav system used information in DRACO images to successfully impact Dimorphos. In all images, Dimorphos north pole (+Z) is toward the bottom left. Images from left to right: dart_0401915351_36903_01_raw.fits, dart_0401925635_06853_01_raw.fits, dart_0401927052_23729_01_raw.fits, and dart_0401929899_33346_01_raw.fits.

Figure 2. The asteroid Dimorphos and the DART impact site as seen in calibrated DRACO images. (a) Dimorphos with an appropriately scaled and correctly oriented outline of the DART spacecraft centered on the impact site. Note the size of the spacecraft relative to the asteroid. The

spacecraft bus was approximately 1.2 x 1.3 x 1.3 meters from which other structures extended, resulting in dimensions of approximately 1.8 x 1.9 x 2.6 meters. The spacecraft also had two large solar arrays that were each 8.5 meters long. (b) A closer view of the DART impact site showing the outline of the spacecraft bus and solar arrays over the DRACO image. Note the positions of the two solar arrays relative to two large boulders, labeled 1 (6.5 m long) and 2 (6.1 m long). This subframe is from an image taken 2.781 seconds before impact. (c) The spacecraft bus hit between boulders 1 and 2, whereas the solar arrays interacted with these boulders. This subframe is from an image taken 1.818 seconds before impact. The arrow at the lower left of panel (a) indicates the direction of Dimorphos +Z (N) axis. The solid white box in (a) shows the location of the image in (b). The dashed gray box in (b) shows the location of the image in (c). Panels (b) and (c) show subimages of the full frame. Image names: (a) dart_0401930039_14119_01_iof.fits, (b) dart_0401930048_45552_01_iof.fits, (c) dart_0401930049_43695_01_iof.fits.

Figure 3. Relationship between the spacecraft and topography at the DART impact site. (a) – (c) show the position of the spacecraft immediately before the impact of the spacecraft bus from different perspectives to visualize the three-dimensional interactions between the spacecraft and surface. In panel (a), Dimorphos north is toward the top of the panel. In panel (b) Dimorphos north is to the right. In panel (c) Dimorphos north is roughly into the page. In all panels, -Y solar array points to Dimorphos north. Length scales vary in these perspective views; the scale bars shown are approximate. Boulders 1 and 2 correspond to boulders 1 and 2 in Figure 2. The caption to Figure 2 gives the spacecraft dimensions.

Methods

Determining the time of impact

The time of impact was computed from spacecraft clock timestamps inserted into each downlinked telemetry frame by the spacecraft's radio. A new telemetry frame was produced every 2.9853 milliseconds with a precision of 20 microseconds. Assuming the impact occurred in the middle of the frame after the final received frame placed the time of impact to within ± half a frame period:

401,930,051.59326 ± 0.00149 s spacecraft clock time

This spacecraft clock time of impact was converted to UTC. This conversion increases the uncertainty slightly:

2022-26-9 23:14:24.183 ± 0.004 s UTC

This time is the UTC of the impact at Dimorphos, not the time on Earth when the last telemetry frame was received. As each DRACO image is timestamped with a spacecraft clock value, the time to impact for each image can be computed with similar accuracy.

Shape modeling of Dimorphos

We built the shape model using stereophotoclinometry (SPC), a technique that has been widely used to model the shape of small bodies[40–42]. Prior to DART's impact, the shape modeling team conducted tests to understand the strengths and limitations of the SPC approach given the data expected from DART[43]. DART images pose a challenge for any image-based shape modeling technique due to the single viewing geometry and lighting condition. SPC provides robust results despite these challenges[43].

Extended Data Fig. 7 illustrates the steps used to build the Dimorphos shape model. First, we used DRACO images to determine the dimensions of an initial triaxial ellipsoid. The ellipsoid was constrained by the location of the sunlit limb, the location of the limb lit by light scattered off Didymos, and the position of the terminator. Together, the sunlit and Didymos-lit limbs revealed the complete extents of the X and Z axes of Dimorphos (Extended Data Fig. 8). The position of the terminator constrained the Y-axis extent. The last DRACO image to contain all of Dimorphos in the field of view was registered to the ellipsoid. Other DRACO images were registered to that image or, in the case of the highest-resolution images of the impact site, to the immediately preceding image. In order to correctly determine the scale of the shape model, we used the known time of impact and spacecraft speed to set the spacecraft range for each image.

Next, we pursued parallel paths (Extended Data Fig. 7). The first path used standard SPC processes to construct small digital terrain models (called “maplets”) using an SPC program called lithos[40,42,43]. Maplets were tiled all across the surface of the asteroid in the areas seen by DRACO. Maplets went through several iterations to compute the maplet topography[40,42,43]. After several iterations, the maplet ensemble was averaged to create a global digital terrain model (DTM). Areas without maplet coverage remained unchanged. This cycle was repeated with maplets of increasingly finer ground-sample distances (GSD) in the areas covered by higher-resolution images surrounding the impact site. The finest-scale maplets had a GSD of 3 cm, comparable to the pixel scale of the final, partial DRACO image. The second path focused on matching the sunlit limb. We built maplets along the sunlit limb that were conditioned by limb points identified in the tilt-to-height integration in an SPC iteration. These maplets were made at only two ground-sample distances due to the coarser resolution of images that contained limb.

Once the topography in the standard maplets and limb-only maplets **stabilized**, we united them via several SPC iterations and proceeded to build the global DTM.

The areas covered by maplets on Dimorphos global DTM are shown in Extended Data Fig. 1 as shaded gray regions. The blue and magenta points show the locations of the sunlit and Didymos-lit limbs. The unseen side of the asteroid is roughly centered on the 90° East view. The shape model has the volume and extents reported in Table 1. The global DTM has a typical GSD of 26 centimeters, but that resolution is only meaningful in the areas covered by maplets.
We also used the standard maplets to construct a DTM of the impact site. The impact site is covered by the highest-resolution images, so the impact site can support finer-scale topography than the global model. The impact site DTM has a GSD of 5 cm and is shown in Figure 3.

Due to the short period of time for which we have resolved images of Dimorphos, the rotation pole, prime meridian, and rotation rate of Dimorphos could not be updated using SPC. Instead, we used values derived by ground-based observers. In the equatorial J2000 frame, the pole values used for Dimorphos are[14]:

BODY120065803_POLE_RA = (60.936309840897856, 0, 0)

BODY120065803_POLE_DEC = (-71.674565992873852, 0, 0)

The coordinate system of the global DTM of Dimorphos has the prime meridian pointed toward Didymos, consistent with IAU convention:

BODY120065803_PM = (64.914870949788195, 724.723943017441570, 1.0840372309e-06)

A planetary constants kernel (PCK) with these values is available at https://ssd.jpl.nasa.gov/ftp/eph/small_bodies/dart/dimorphos/archive/ called "dimorphos_s501-preimp.tpc". Documentation for PCK files, including units for the terms listed above, is available here: https://naif.jpl.nasa.gov/pub/naif/toolkit_docs/FORTRAN/req/pck.html#Text%20PCK%20Kernel%20Variable%20Names. Dimorphos's north pole is in the +Z direction of the shape model but oriented toward ecliptic south.

Shape model uncertainties

We quantified uncertainties in the global DTM of Dimorphos using techniques employed to estimate the uncertainties associated with the global DTM of Bennu[44]. These techniques were also used to assess uncertainties in shape models developed during pre-impact tests done for DART[43]. The analyses involved comparing DRACO images against the global DTM when rendered with the same lighting and viewing geometry as the image. We used three analyses described in the above references. The first method, referred to as the limb/terminator method, used image thresholding to identify limb and terminator in the DRACO image and rendered shape model. The thresholded images were subtracted to reveal mismatches between the image and rendered shape model and any size bias in the model (Extended Data Fig. 9a-9e). The second and third methods relied on analysis of corresponding surface features, or keypoints, in images and the rendered shape model, to understand errors in the overall size of the shape model (Extended Data Fig. 9**f-9i**). In the second method, referred to as keypoint matching, the rendered image was rotated, translated, and scaled to minimize differences in keypoint locations on the DRACO image and rendered shape model. The third method, referred to as keypoint distance,

was based on the measured distances between all keypoints in the DRACO image and rendered shape model.

The limb/terminator assessments indicated that the model is 75 cm too small in X, Y, and Z, with a limb uncertainty of 1.3 – 2 m. Most of the mismatch between DRACO images and the rendered shape model occurred along the limb and terminator. We expected larger uncertainties in these areas due to the limited coverage and single lighting condition in DRACO images. The keypoints indicated that the Dimorphos shape model is 6 ± 29 cm too large and that features in the model have point-separation errors of -11 ± 20 cm. The keypoint assessments indicated that the model performed well in areas where DRACO resolved detailed surface features, which is the area of the model that is most relevant to understanding the topography of the impact site. Comparisons between shadow lengths in DRACO images and shadow lengths in shape model renderings indicated that some boulder heights are too small. This mismatch was expected based on shape modeling tests done for DART and is a consequence of constructing the shape model from a single lighting condition and viewing geometry[43]. Shadow lengths suggest that height of boulder 1 in the impact site DTM is ~10% too small, but the height of boulder 2 in the impact site DTM is correct. Based on all of these analyses, we assumed uncertainties of two meters in the extents of Dimorphos in the X and Z directions.

Because DRACO saw a complete outline of the asteroid (Extended Data Figure 8) and the spacecraft approach geometry was such that this outline was primarily in the X-Z plane, the shape model dimension uncertainties in X and Z are less than 1% (Table 1). Hence, the Y-axis extent is the largest source of uncertainty in the volume. Future work will refine the errors in the

Y-axis, but for the time being we assume the uncertainty in Y is two times the uncertainties in X and Z (i.e., 4 meters).

Measuring the volume of Dimorphos and realistically estimating uncertainties on that quantity is of particular interest because it directly affects our understanding of the mass of the asteroid. In the shape modeling tests[43], we took scaled shape models of an ellipsoid, Itokawa, and Bennu, rendered a set of simulated DRACO images from the "truth" shape models, and then used SPC to build shape models from simulated images[43]. We compared the volumes of the models built using SPC against the volumes of truth models[43]. The volume errors in those tests ranged from -2% to +23% [43]. The test with the lowest volume error was for an ellipsoidal asteroid. The roughly ellipsoidal shape of Dimorphos as seen by DRACO suggests that the volume error in the Dimorphos global DTM is likely on the order of several percent, rather than 23%, by virtue of the simplicity of Dimorphos's long-wavelength shape. Moreover, in the tests with the largest volume errors, the terminator of the shape model—which is the primary constraint on the extent of the shape into and out of the page—did not match the terminator of the original images. In the case of Dimorphos, the terminator matched nicely between the global DTM and the rendered shape model (Extended Data Figure 9). Given the results from the shape modeling tests[43], this agreement indicated that the volume errors for Dimorphos are likely on the order of several percent. Based on these assessments, a volume error of 5% seems probable. But, we adopted a volume uncertainty of 10% to be conservative. This volume error is larger than the value implied by the reported uncertainties in the X, Y, and Z extents, but the intent is to be conservative.

Shape modeling of Didymos

A preliminary SPC shape model of Didymos was built from DRACO data. This model led to the preliminary volume and extent of Didymos reported in Table 1. DRACO images revealed a smaller Z-axis and showed that the visible portion of the X-axis likely needs to be extended by a few tens of meters compared to a radar-derived shape model[12]. We used the techniques employed to estimate shape model uncertainties described in the "Shape modeling of Dimorphos" section to assess the preliminary SPC shape model of Didymos. Because the full X- and Z-extents of Didymos cannot be measured in DRACO images (in contrast to Dimorphos), we conservatively attributed an uncertainty of 15 m to the lengths of all the axes of Didymos.

Impact site identification

The construction of an SPC shape model produced a set of surface landmarks that were used to determine the location (at the time of each image) of the spacecraft relative to the surface in the Dimorphos body fixed frame. This procedure used the spacecraft's Didymos relative velocity computed by the ground navigation team using a combination of radiometric tracking data (Doppler, range) and optical images of Didymos. We used this information and the shape model of Dimorphos to compute the location of the impact site. The positions of the DART spacecraft from SPC were converted to the inertial J2000 frame and corrected for light time and aberration. The velocity of the spacecraft was estimated by fitting a second-order polynomial function to these positions as a function of time. This approach is identical to that employed previously[45] to estimate the position of the Hayabusa spacecraft relative to Itokawa. We used the locations from the last 14 complete images collected by DART to determine the spacecraft velocity. These images contained large numbers of landmarks due to their fine pixel scales, which help anchor

the spacecraft position for each image. The fit residuals (i.e., the difference between the fit of the spacecraft location to that determined from SPC) are < 1m (Extended Data Figure 10).

We combined our estimated velocity and the SPC-derived spacecraft positions of the last five images to determine the impact location. Only the last five images were used to locate the impact because heater cycling on the spacecraft introduced cyclic error rates in the inertial attitude knowledge. These rates were estimated to be small at the time of impact due to the timing of impact relative to heater cycling but at their highest approximately 30 seconds prior to impact. Using only the last few images reduced the influence of this known (and cumulative) error source. At each of these five spacecraft positions, we propagated the velocity vector until it intersected with the surface of the Dimorphos shape model. We took the mean of these positions as the impact location. We also computed the spacecraft state at a few different heights above the intersection point in order to determine the order in which the solar arrays and bus contacted the surface. The propagation from each of the last five images provided the same impact point to within 1 cm. The uncertainties in the impact point location (reported in Table 1) are dominated by the residuals to the fits of the spacecraft position obtained by SPC in the Y and Z directions (Extended Data Figure 10).

Impact angle assessments

The tilt angle of the surface relative to the impact velocity vector defines the impact angle. Because the impact site DTM resolves topography at a 5-cm GSD, the spacecraft bus **would have interacted with on the order of a thousand** facets of the DTM. Therefore, we calculated a mean tilt with respect to the impact velocity vector for each facet in the impact site DTM. The

mean tilt calculation is based on previous work[41]; however, we computed mean tilt with respect to the impact velocity vector, *v,* rather than the radial vector to a given facet to determine the impact angle.

The magnitude of the mean tilt for a facet at the impact point is the angle between *v* and the average normal, $\boldsymbol{n}_{\mathbf{av}}$, which is the weighted average of the normal vectors of all facets in the user-defined region, $\boldsymbol{n}_{\mathbf{av}}=\sum(\boldsymbol{n}_{\mathbf{i}}\, A_{\mathrm{i}})/\sum A_{\mathrm{i}}$ surrounding the impact point. In this study, this region was 1.5 m in radius in order to exceed the size of the spacecraft bus. The normal vector of each facet in the region of interest, $\boldsymbol{n}_{\mathrm{i}}$, was weighted by A_{i}, the area of the facet projected onto a best-fit plane to the region selected to determine the surface tilt. This yields a mean tilt = $\mathrm{acos}(n_{\mathrm{av}} \cdot v / |n_{\mathrm{av}}||v|)$. Impact angle, θ, which is typically defined relative to the local horizontal for planetary impacts, is given by θ =90-(mean tilt). The impact angle shown in Table 1 is computed from the mean tilt and θ of the facet closest to the impact point.

As discussed in the "Impact site identification" section, the location of the impact site has an uncertainty of ±68 cm. To understand the range of mean tilts that DART may have encountered given the uncertainty in the impact location, we considered the distribution of mean tilt for all facets within a circle with radius 68 cm centered on the impact site (Extended Data Figure 2). The standard deviation of this distribution was 7° (one sigma), which we attributed as the uncertainty of the impact angle DART may have experienced.

Boulder Counting

The longest axis of each boulder in the final full DRACO image was identified as a line (as done for asteroid (101955) Bennu[46]. The length of the longest axis was determined from the line length and image pixel scale, assuming the last full image as a "flat" scene. The total number of boulders and pebbles identified in the final full DRACO image impact site is 953 and range in size (that is, length of the longest axis) from 0.16 (limit of image resolution, assuming ≥3 pixel sampling[47]) to 6.5 m. The resulting size–frequency distribution is presented in Extended Data Figure 6.

Estimates for the density of Dimorphos

To first order, the combined system mass, M_{sys}, was estimated using Kepler's 3rd law,

$$M_{sys} = (4\pi^2 a^3)/(GP^2)$$

where a and P are the pre-impact semimajor axis and orbit period, and G is the gravitational constant. Neglecting the aspherical shapes of Didymos and Dimorphos and their associated gravitational potentials may lead to an overestimate of the system mass by ~1-2%[48]. However, this error is negligible as the uncertainty in Dimorphos's semimajor axis dominates the uncertainty in the system mass. Next, the bulk density of the combined system was obtained by dividing the system mass with the combined volume of both bodies,

$$\rho_{sys} = (3M_{sys})/(4\pi[R_A^3+R_B^3])$$

where R_A and R_B are the respective volume-equivalent radii of Didymos and Dimorphos. Based on the pre-impact orbit period and semimajor axis[6], and the volume-equivalent diameters provided in this work, we calculated a nominal system bulk density of 2400 ± 250 kg/m^3 using the uncertainties quoted in the previous sentence. However, in order to represent additional possible systematic uncertainties, we adopted a slightly larger uncertainty, which gives a system bulk density of 2400 ± 300 kg/m^3.

The porosity of Dimorphos was estimated as follows:

$$\phi=1-(\rho_{bulk}/\rho_{grain})$$

In this work, we assumed that Dimorphos's bulk density matches the entire system's bulk **density**. There are three NEA systems for which the satellite's bulk density has been independently measured: 66391 Moshup, 2000 DP107, and 2001 SN263 (two satellites). Two of those satellites (Squannit and 2001 SN263 gamma) were measured to be denser than the primary and two were less dense (2001 SN263 beta and 2000 DP107 beta)[20–22]. For all three systems, the 1-sigma uncertainties for the satellite and the primary densities overlap. Furthermore, **recent work** [49] estimated that the size of Squannit is about 30% larger than estimated previously[20], meaning that the bulk density of Squannit may be in better agreement with its primary. Given these other examples, assuming Dimorphos's density matches the system bulk density is a reasonable starting point, although its true density could differ significantly from this value. Hera will determine the masses and densities of Didymos and Dimorphos and test the validity of this assumption[39].

Methods references

40. Gaskell, R. W. *et al.* Characterizing and navigating small bodies with imaging data. *Meteorit. Planet. Sci.* **43**, 1049–1061 (2008).

41. Barnouin, O. S. *et al.* Digital terrain mapping by the OSIRIS-REx mission. *Planet. Space Sci.* **180**, 104764 (2020).

42. Palmer, E. E. *et al.* Practical Stereophotoclinometry for Modeling Shape and Topography on Planetary Missions. *Planet. Sci. J.* **3**, 102 (2022).

43. Daly, R. T. *et al.* Shape Modeling of Dimorphos for the Double Asteroid Redirection Test (DART). *Planet. Sci. J.* **3**, 207 (2022).
44. Al Asad, M. M. *et al.* Validation of Stereophotoclinometric Shape Models of Asteroid (101955) Bennu during the OSIRIS-REx Mission. *Planet. Sci. J.* **2**, 82 (2021).
45. Barnouin-Jha, O. S. *et al.* Small-scale topography of 25143 Itokawa from the Hayabusa laser altimeter. *Icarus* **198**, 108–124 (2008).
46. Burke, K. N. *et al.* Particle Size-Frequency Distributions of the OSIRIS-REx Candidate Sample Sites on Asteroid (101955) Bennu. *Remote Sens.* **13**, 1315 (2021).
47. Pajola, M. *et al.* Size-frequency distribution of boulders ≥7 m on comet 67P/Churyumov-Gerasimenko. *Astron. Astrophys.* **583**, A37 (2015).
48. Agrusa, H. F. *et al.* The excited spin state of Dimorphos resulting from the DART impact. *Icarus* **370**, 114624 (2021).
49. Scheirich, P. *et al.* A satellite orbit drift in binary near-Earth asteroids (66391) 1999 KW4 and (88710) 2001 SL9 — Indication of the BYORP effect. *Icarus* **360**, 114321 (2021).

Extended data figures

Extended Data Fig. 1. The Dimorphos global digital terrain model (DTM) as viewed along its principal axes. The black star marks the DART impact site. Colors on the DTM indicate the various constraints used to build the model.

Extended Data Fig. 2. Tilts and topography at the impact site. DTM of the DART impact site with facets colored by the impact angle with respect to local horizontal, averaged over a 3-m region. The DTM is lit to match the lightning in DRACO images at the time of impact. The

white circle shows the uncertainty in the impact location (a circle with a radius of 68 cm). Boulders 1 and 2 correspond to boulders 1 and 2 in Figure 2. (b) The same DTM with DRACO image dart_0401930048_45552_01_iof.fits draped over it. The image does not cover the entire DTM, so the corners of panel b show the impact angle plate coloring. (c) Histogram of tilts within the white circle representing the uncertainty in the impact site location. (d) – (g) Perspective views of the impact site DTM with overlaid image shown in (b), i.e., the DTM in panel (b) viewed edge on from each of the four sides of the DTM. Boulders 1 and 2 are prominent, as is the small niche between them in which the spacecraft bus hit the surface.

Extended Data Fig. 3. Boulders at the impact site. (a) Zoomed-in view of the impact site DTM to focus on the two largest boulders near the impact site. Facets in the DTM are colored by the height of the facet along a normal to a plane fit to all of the points in the DTM. DRACO image dart_0401930048_45552_01_iof.fits is draped over the DTM at 40% opacity. The DTM is lit to match the lightning in the DRACO image. The white circle shows the uncertainty in the impact location (a circle with a radius of 68 cm). The red and blue paths show the locations of two topographic profiles across (b) boulder 1 from A to A' and (c) boulder 2 from B to B'.

Extended Data Fig. 4. Dimorphos and Didymos as seen by DART. (a) The asteroid Dimorphos seen at a range of pixel scales. Numerous boulders can be distinguished across the surface in images as coarse as 2–3 m pixel scale. Without the context of higher-resolution images, it would be difficult to definitively identify boulders in the 4-m pixel scale image. Image names (from left to right): dart_0401929985_18096_01_iof.fits, dart_0401929952_31226_01_iof.fits, dart_0401929919_44355_01_iof.fits. (b) Composite image

of asteroids Dimorphos and Didymos. Dimorphos is at left; Didymos is at right. The two asteroids and the distance between them are to scale. This image was produced by combining two DRACO images to show Dimorphos at higher resolution than Didymos. In spite of the different resolutions, the two surfaces give different first impressions. Dimorphos has a boulder-rich surface with an ellipsoidal shape. Didymos exhibits boulders but also smoother areas and larger concavities. **The north poles of Dimorphos and Didymos point to the top of the figure.**

Extended Data Fig. 5. The final full DRACO image of Dimorphos's surface. Examples of cracks (white arrows), rocks on rocks (squares) and a partially buried boulder are indicated. Image name: dart_0401930049_43695_01_iof.fits. The north pole of Dimorphos is toward the top of the figure.

Extended Data Fig. 6. The size-frequency distribution of boulders identified in the last DRACO full image (dart_0401930049_43695_01_iof.fits). The limit of image resolution, assuming ≥3 pixel sampling, is ~16.5 cm, so the overturn at small sizes is real and not an observational bias (Pajola et al. 2015). Here, a conservative 5-pixel sampling limit (27.5 cm) is indicated by the vertical blue dashed line. The distribution is not well described by a single power law (shown here as a red dot-dashed line with a slope of -1.65).

Extended Data Fig. 7. Shape modeling process used to build a global digital terrain model of Dimorphos. The process was informed by shape modeling tests conducted prior to impact.

Extended Data Fig. 8. Sunlit and Didymos-lit limbs of Dimorphos. The same image of Dimorphos stretched to optimize (a) the limb lit by the Sun and (b) the limb lit by light reflected off Didymos. In (b), pixels with I/F < 0.014 have been scaled up by a factor of 6 to allow the faint features to be seen along with the sunlit features, for better comparison to (a). Together, the two limbs reveal a complete outline of the asteroid as seen by DRACO. The image is dart_0401930039_14119_01_iof.fits.

Extended Data Fig. 9. Shape model assessments. (a) – (e) show results from limb/terminator shape model assessments. Panels (a) – (c) show an example of (a) a reference DRACO image, (b) the rendered shape model with the same lighting and viewing geometry as the reference image, and (c) the difference between the model and the reference image. (d) and (e) show results from limb/terminator assessments from many DRACO images. (d) Sum of the absolute value of the image-model differences, normalized by the image perimeter. The median is the most relevant measure of uncertainty from this metric because the distribution is always one-sided and never gaussian. (e) The differences in the radii of the equivalent-area circles for the reference image and rendered shape model, respectively. The radius of the equivalent-area circle is the radius of a circle with the same area as the total area of lit terrain on either the rendered model or the reference image. The mean is the most relevant measure of uncertainty from this metric because the distribution should be symmetric. (f) – (i) show results from keypoint assessments. The colored lines in panels (f) and (g) connect features matched by the algorithm in the image and on the shape model. Most, but not all, matches are reasonable, so the median value based on all keypoints is used. (h) shows a metric derived from differences between corresponding keypoints across several tens of DRACO images. (i) shows a model-to-image

scale factor derived by comparing the distances measured between all keypoints in the reference DRACO image to the distances measured between all keypoints in images of the rendered shape model. The arrows in panels (a) and (g) indicate the direction of Dimorphos north (+Z).

Extended Data Fig. 10. Fit residuals. (a) Spacecraft position residuals and (b) residual distributions estimated after fitting the spacecraft locations obtained during the SPC shape modeling process with a second-order polynomial all in the J2000 inertial frame relative to Dimorphos. Uncertainties attributed to the location of the impact site and reported in Table 1 are in the Y and Z axes.

Data availability

The DRACO images shown in this paper, the global digital terrain model of Dimorphos, and the local digital terrain model of the impact site are available in a permanent archive associated with this paper in the JHU/APL Data Archive (https://lib.jhuapl.edu/papers/dart-an-autonomous-kinetic-impact-into-a-near-eart/). All raw and calibrated DRACO images, as well as higher-order products such as digital terrain models, will ultimately be available via the Planetary Data System (PDS) (https://pds-smallbodies.astro.umd.edu/data_sb/missions/dart/index.shtml) by October 2023.

Acknowledgements

We thank Paul Boie, Ray Harvey, Mark Hill, Andrew Johnson, Cindy Kim, Jong Kim, Daniel O'Shaughnessy, Nadja Osiander, Geffrey Ottman, Lev Rodovskiy, Matthew Rodriguez, Andrew Smith, Kirk Volland, and all of the other people who made the DART impact possible. We thank

Megan Bruck Syal and Kathryn Kumamoto for their feedback on the manuscript. This work made use of the Small Body Mapping Tool.

This work was supported by the DART mission, NASA Contract No. 80MSFC20D0004. This work was supported by the Italian Space Agency (ASI) within the LICIACube project (ASI-INAF agreement AC n. 2019-31-HH.0). P.S. and P.P. were supported by the Grant Agency of the Czech Republic, grant 20-04431S. B.J.B. was funded by the NASA DART Participating Scientist Program #20-DARTPSP20-0007. S.C. acknowledges funding from the Crosby Distinguished Postdoctoral Fellowship Program of the Department of Earth, Atmospheric and Planetary Science, Massachusetts Institute of Technology. G.S.C. was funded by UK Science and Technology Facilities Council Grant ST/S000615/1. F.F. acknowledges funding from the Swiss National Science Foundation (SNSF) Ambizione grant No. 193346. M.J. and S.D.R. acknowledge support by the Swiss National Science Foundation (project number 200021_207359), and from the European Union's Horizon 2020 research and innovation programme under grant agreement No. 870377 (project NEO-MAPP). T.K. is supported by Academy of Finland project 335595 and by institutional support RVO 67985831 of the Institute of Geology of the Czech Academy of Sciences. P.M. acknowledges funding support from the European Union's Horizon 2020 research and innovation program under grant agreement No. 870377 (project NEO-MAPP), the CNRS through the MITI interdisciplinary programs, CNES and ESA. N.M. and C.Q.R. acknowledge funding support from the European Commission's Horizon 2020 research and innovation programme under grant agreement No 870377 (NEO-MAPP project) and support from the Centre National d'Etudes Spatiales (CNES). J.O. has been funded by grant No. PID2021-125883NB-C22 by the Spanish Ministry of Science and

Innovation/State Agency of Research MCIN/AEI/ 10.13039/501100011033 and by "ERDF A way of making Europe". S.R.S. acknowledges support from the NASA DART Participating Scientist Program, award no. 80NSSC22K0318. J.K.S. acknowledges support from NASA award 80NSSC21K1014. J.M.T.-R. acknowledges financial support from the Ministerio de Ciencia e Innovación—Agencia Estatal de Investigación (PID2021-128062NB-I00). P.B. acknowledges funding support from Europlanet/University of Edinburgh and Technical University of Kenya. Part of this research was carried out at the Jet Propulsion Laboratory, California Institute of Technology, under a contract with the National Aeronautics and Space Administration.

Author contributions

R.T.D., C.M.E., and O.S.B. jointly led the writing of this paper, identification of the impact site, and shape modeling of Dimorphos. R.T.D is the Dimorphos shape modeling lead. C.M.E. is the DRACO instrument scientist. O.S.B. is the Proximity Operations Working Group lead. N.L.C., A.S.R. and A.F.C. lead the DART Investigation Team, contributed to writing and revision of this paper, and coordinated inputs across the DART Investigation Team. E.Y.A. contributed substantial revisions to the manuscript and was the DART mission systems engineer. H.F.A. wrote portions of the manuscript and played a key role in the analysis and interpretation of DART data. E.D.A., A.L.A., J.A.A., A.R.B., D.L.B., J.B., S.B., M.H.C., G.C., M.W.C., P.S.E., A.S.F., Z.J.F., **S.H.,** M.A.H., P.A.H.-D., P.M.H., S.N.J., M.A.J., J.W.J., T.O.K., F.E.L., D.M.M., M.E.M., I.W.M., J.R.R., E.L.R., J.E.R., L.M.Rodriguez, L.M.Roufberg, B.P.R., C.A.S., M.P.S., B.N.S., C.E.S., E.J.S., E.A.S., Z.B.T., J.R.T., B.T.T., A.T.V., D.V., D.S.W., and K.A.W. played integral roles in the engineering team to ensure DART intercepted Dimorphos. R.W.G., M.A.J., and H.N. contributed to the effort to identify the impact site. R.W.G. also assisted with shape

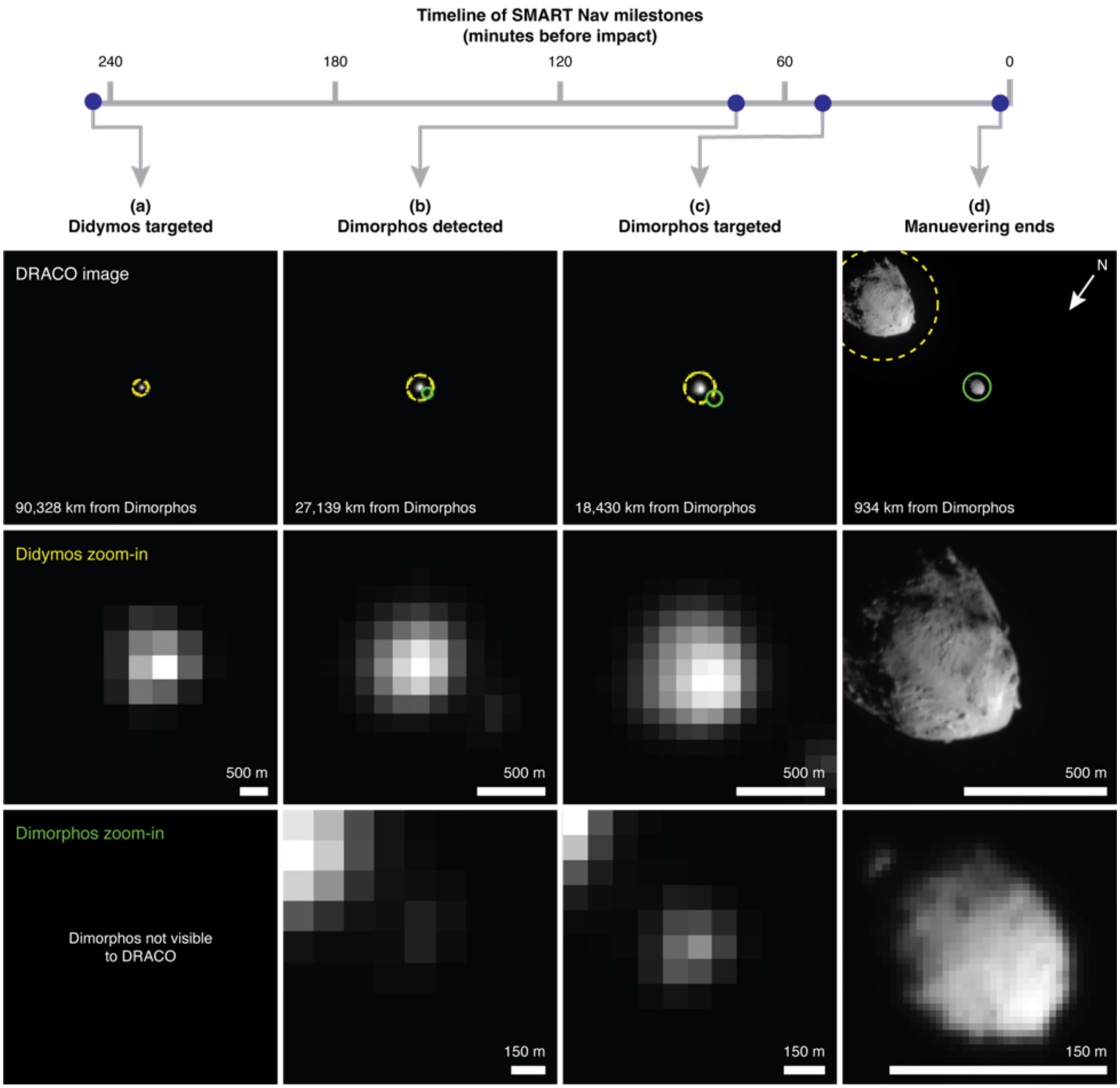
modeling of Dimorphos. E.E.P. led the efforts to use DRACO images to determine the shape of Didymos, with inputs from O.S.B., and R.W.G. B.J.B. calculated the geometric albedo of Didymos. T.L.F. contributed to the calibration of DRACO and shape modeling efforts. D.S.W. led determination of the time of impact and wrote that part of the methods section. R.C.E., H.N., and C.D.W. developed the software used to process DRACO images and digital terrain models into data products. S.-Y.W.H. contributed to DRACO calibration. A.L., N.M., M.P., S.D.R., C.Q.R., A.M.S., D.M.G., M.E.D., and J.M.S. contributed to impact site characterization. T.K., H.F.A., M.C.N., D.J.S., J.M.T.-R., Y.Z. contributed to the calculation and interpretation of the density of Dimorphos. S.R.C., N.A.M., S.P.N., C.A.T., P.P., and P.S. provided orbit solutions used to compute the GM of the Didymos system. E.I.A., P.B., R.-L.B., S.C., G.S.C., F.F., D.M.G., I.H. M.H., S.A.J., M.J., R.L., P.M., S.M., M.C.N., J.O., **K.T.R.,** D.J.S., S.R.S, and J.K.S. provided comments that substantively revised the manuscript. This work made use of the Small Body Mapping Tool (SBMT; sbmt.jhuapl.edu). R.J.S., J.M.P., and N.R.L. are the software developers for the SBMT. C.M.E., O.S.B., R.T.D., and A.C.M. also work on the SBMT team.

Competing interests

The authors declare no competing interests

Additional information

Correspondence and requests for materials should be addressed to Dr. Terik Daly (terik.daly@jhuapl.edu).



Timeline of SMART Nav milestones
(minutes before impact)
240
180
120
60
0
(a)
Didymos targeted
(b)
Dimorphos detected
(c)
Dimorphos targeted
(d)
Manuevering ends
DRACO image
N
90,328 km from Dimorphos
27,139 km from Dimorphos
18,430 km from Dimorphos
934 km from Dimorphos
Didymos zoom-in
500 m
500 m
500 m
500 m
Dimorphos zoom-in
Dimorphos not visible
to DRACO
150 m
150 m
150 m

Figure 1

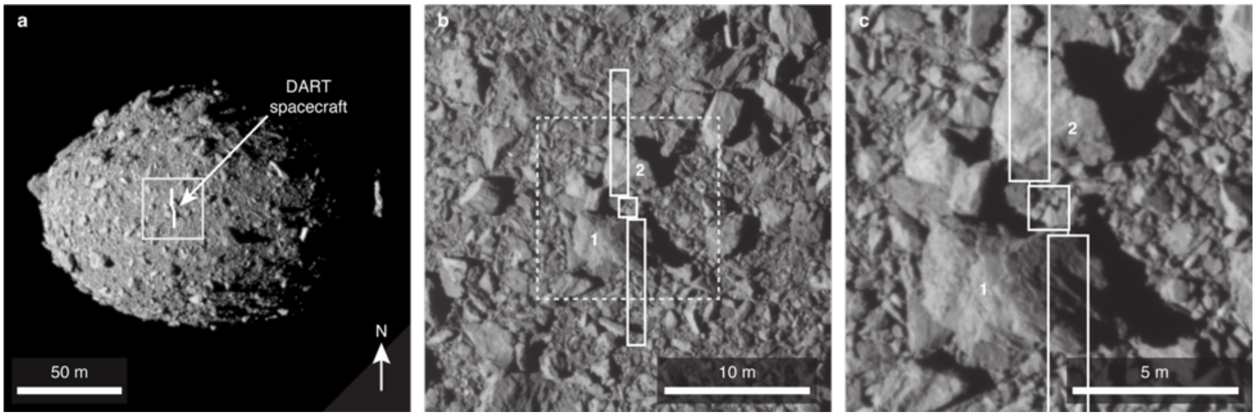


Figure 2

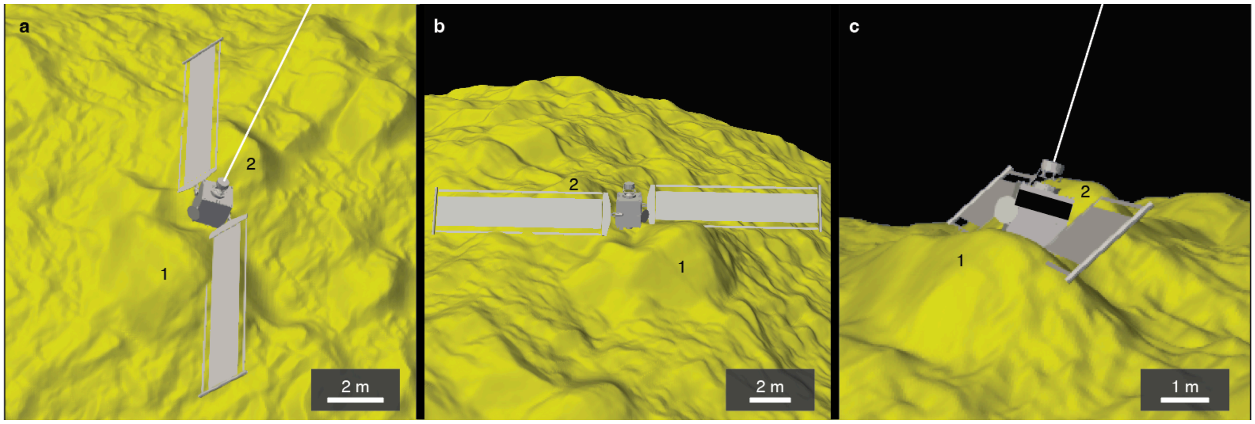
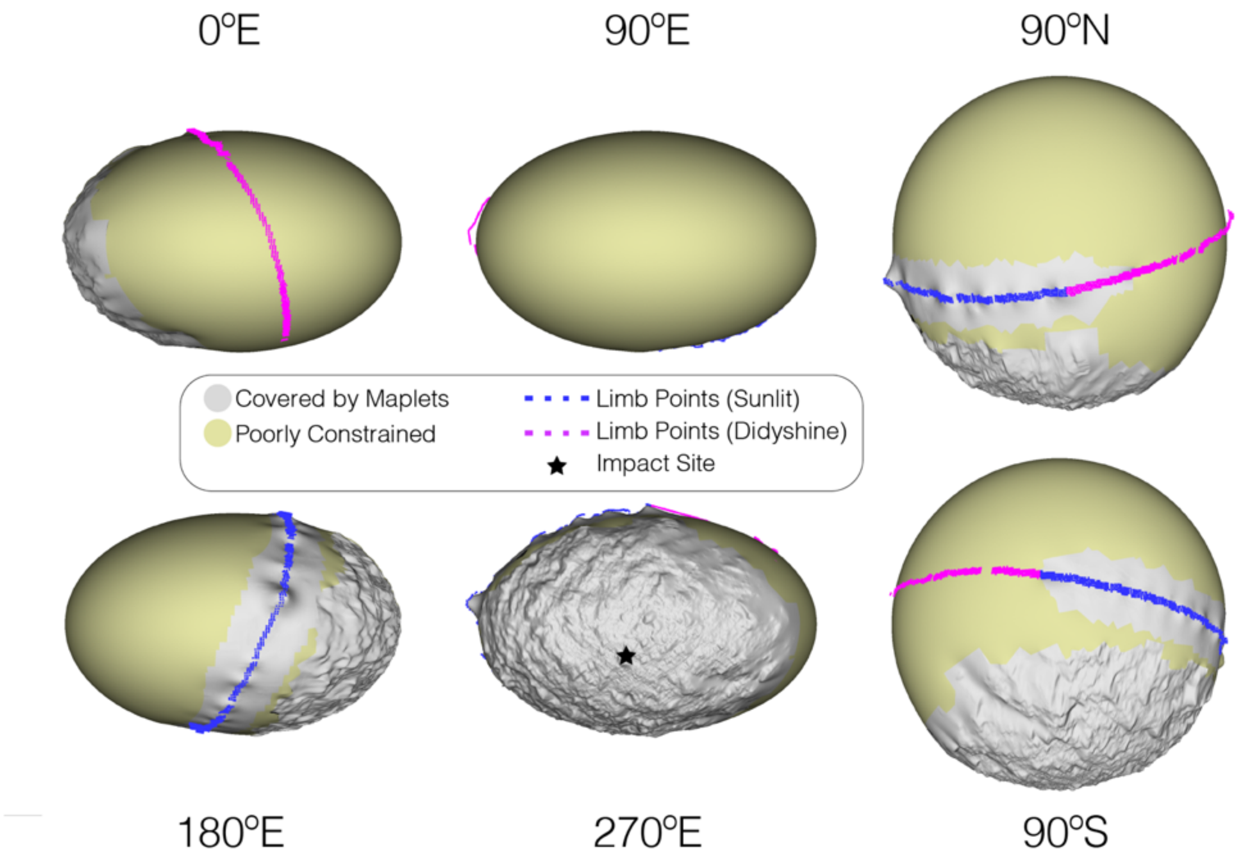
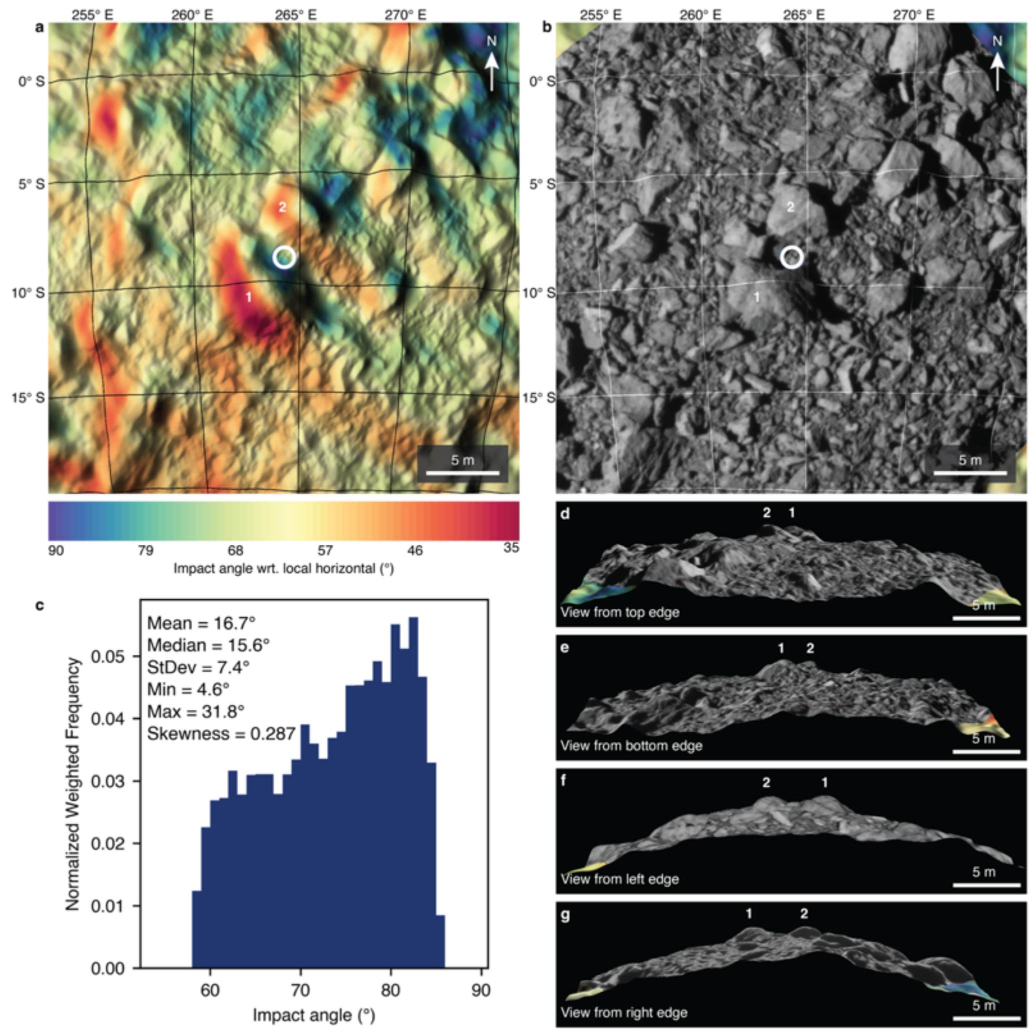


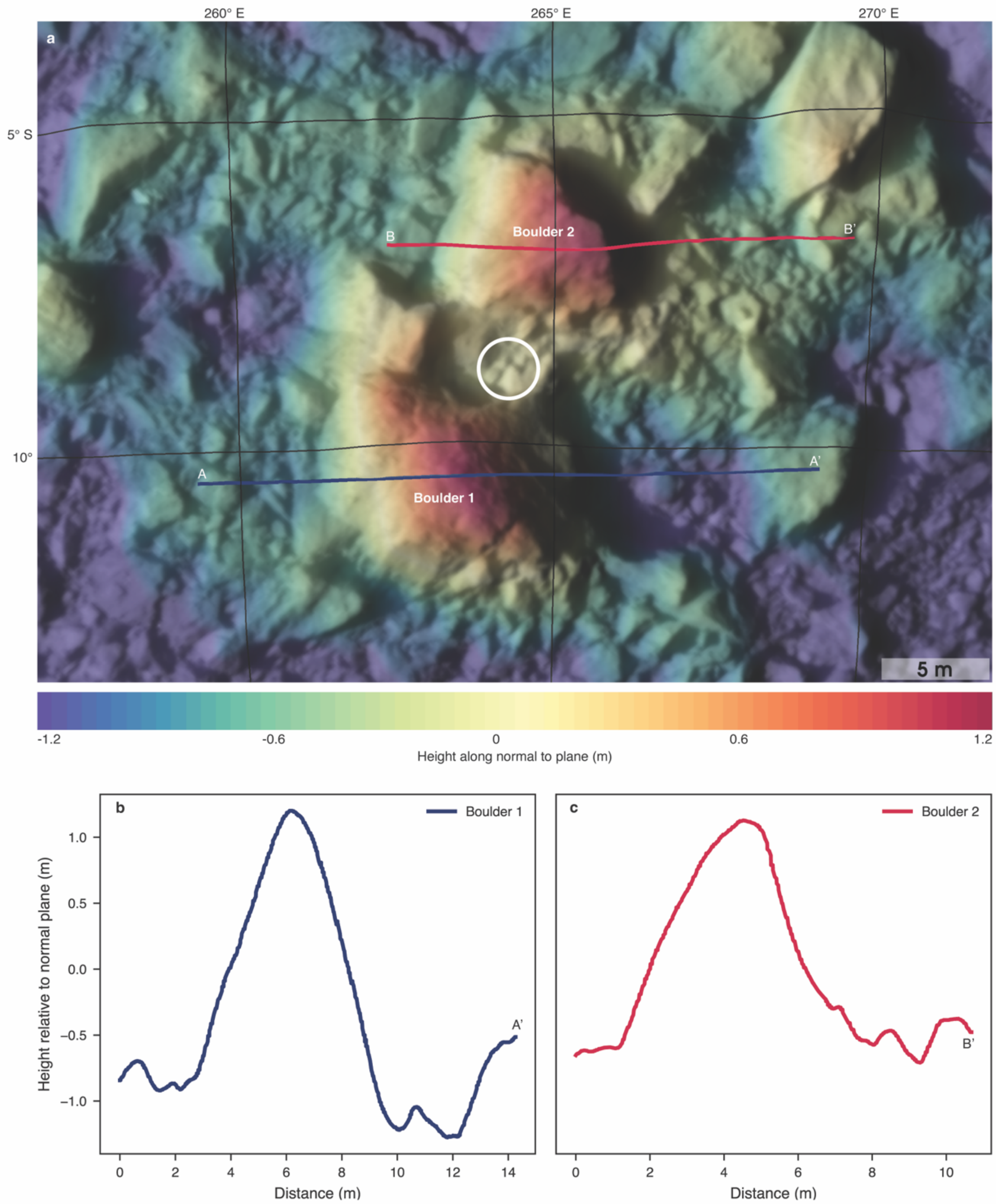
Figure 3



Extended Data Figure 1

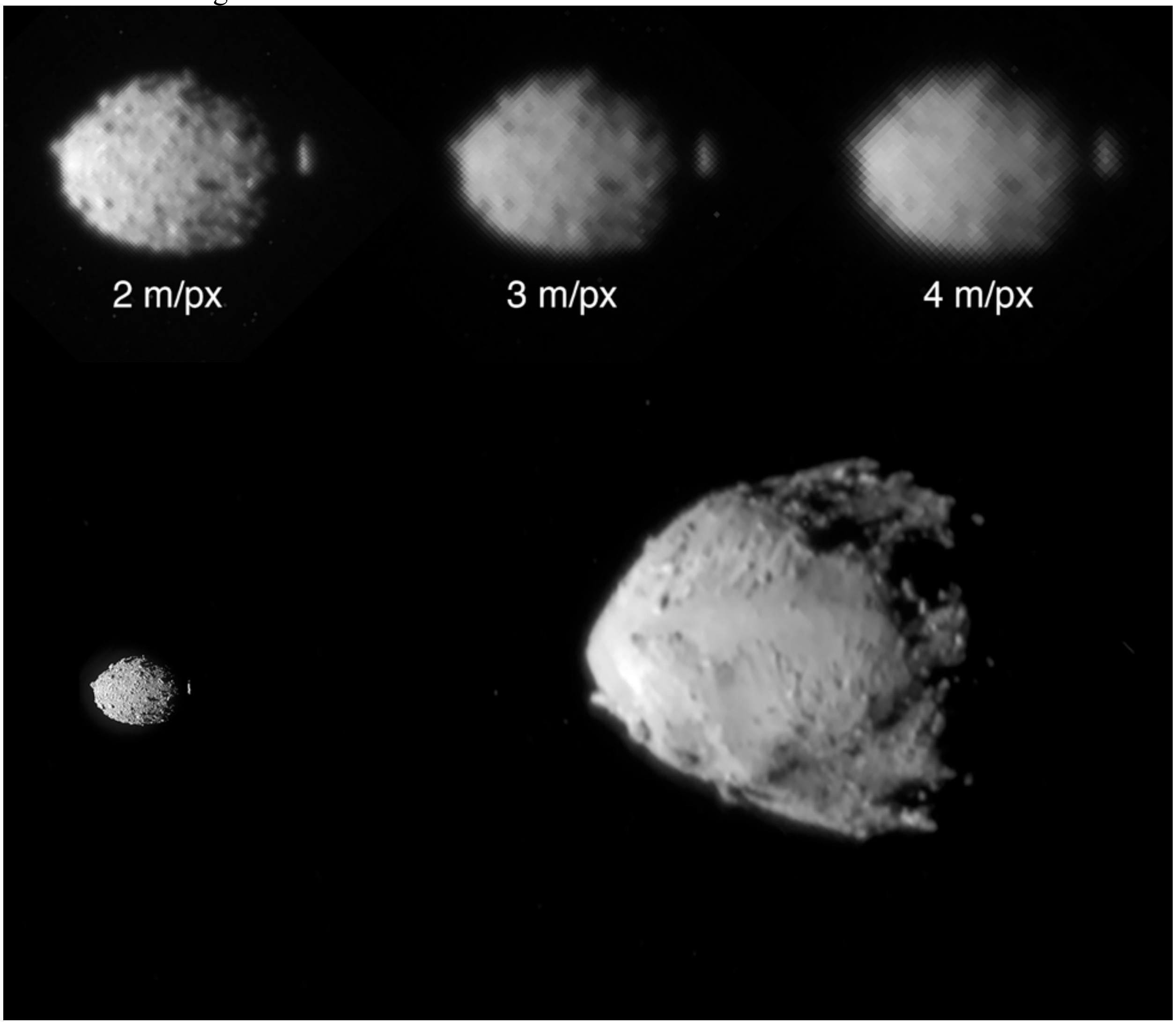


Extended Data Figure 2

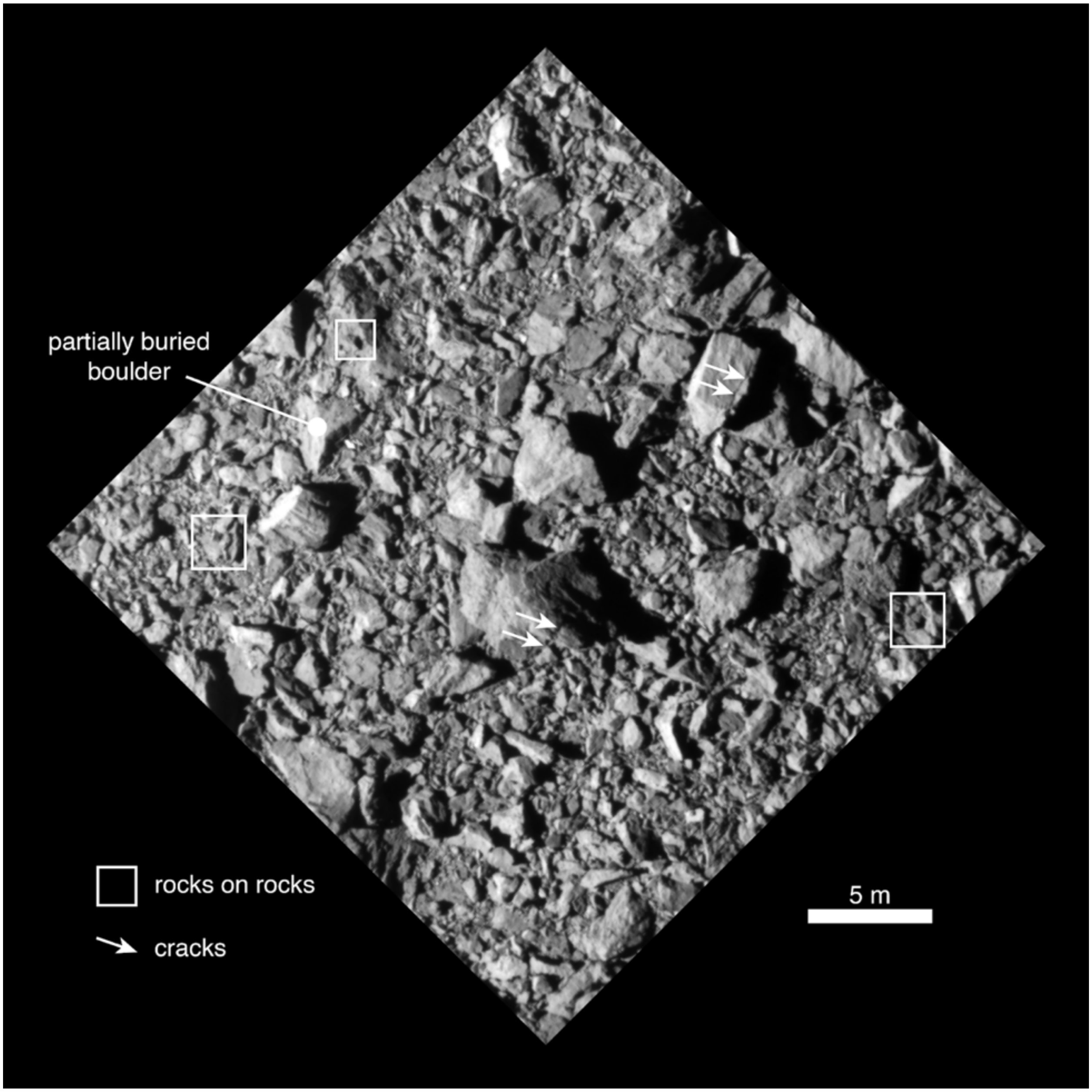


260° E
265° E
270° E
a
5° S
10°
B
Boulder 2
B'
A
A'
Boulder 1
5 m
-1.2
-0.6
0
0.6
1.2
Height along normal to plane (m)
b
Boulder 1
Height relative to normal plane (m)
1.0
0.5
0.0
−0.5
−1.0
A'
0
2
4
6
8
10
12
14
Distance (m)
c
Boulder 2
B'
0
2
4
6
8
10
Distance (m)

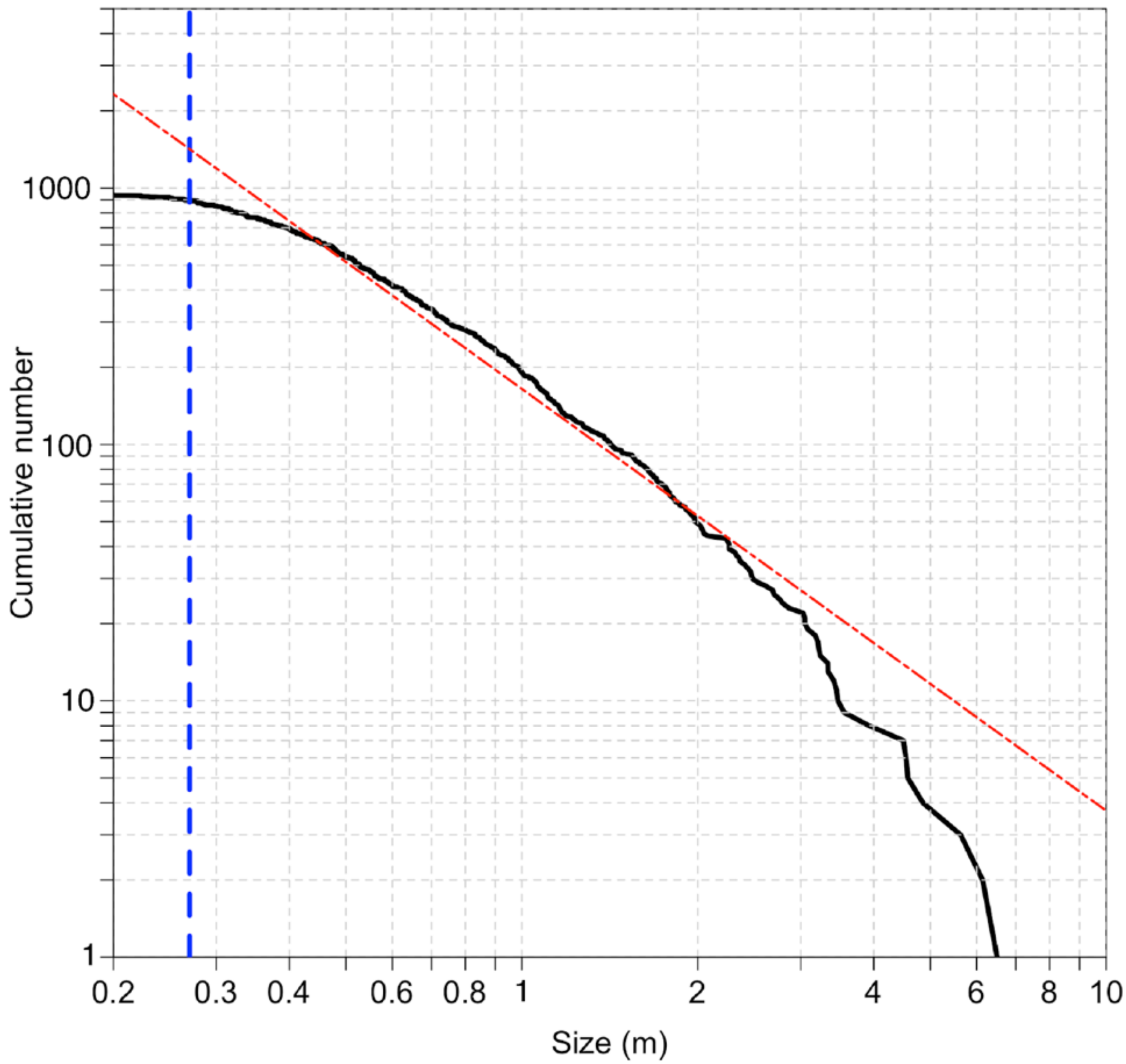
Extended Data Figure 3



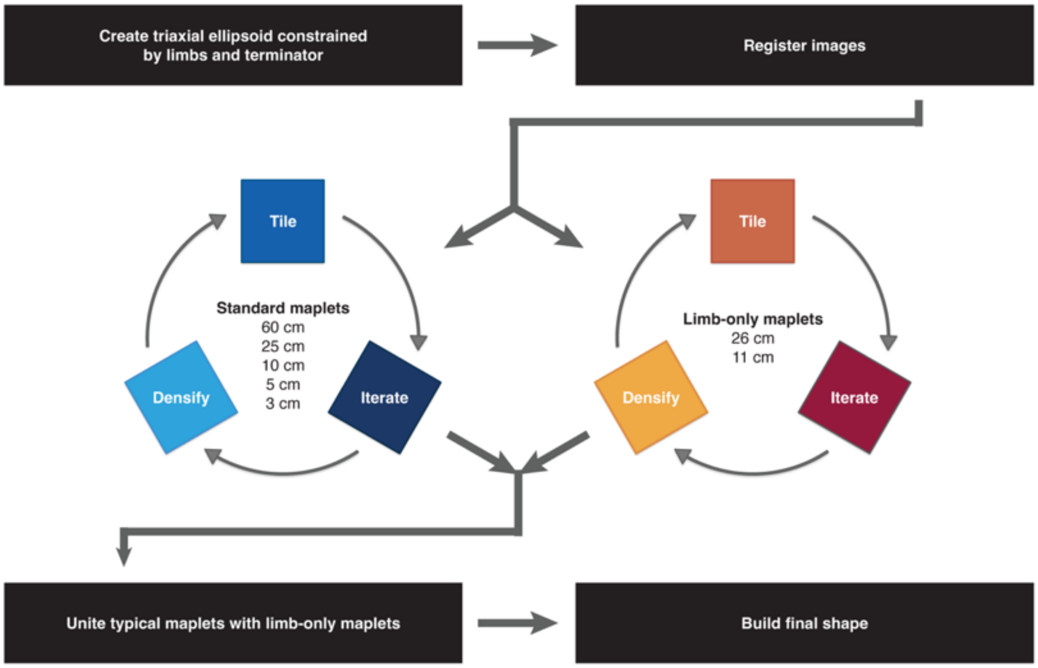
Extended Data Figure 4 = Carolyn will add labels and panel markings to this.



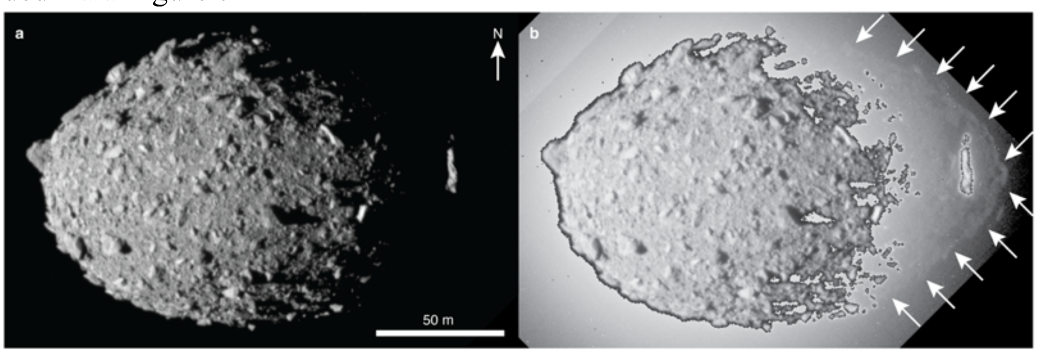
Extended Data Figure 5.



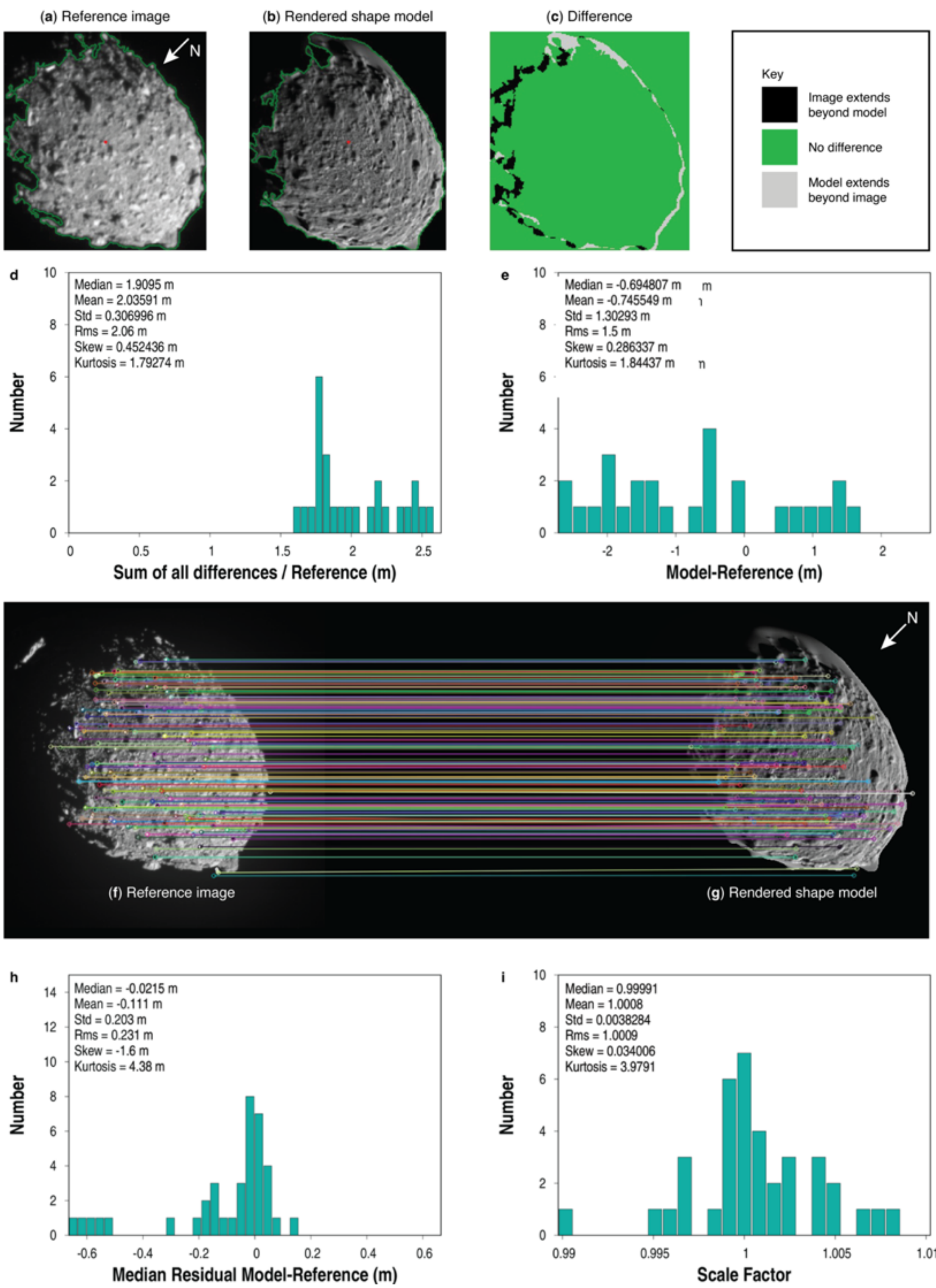
Extended Data Figure 6.



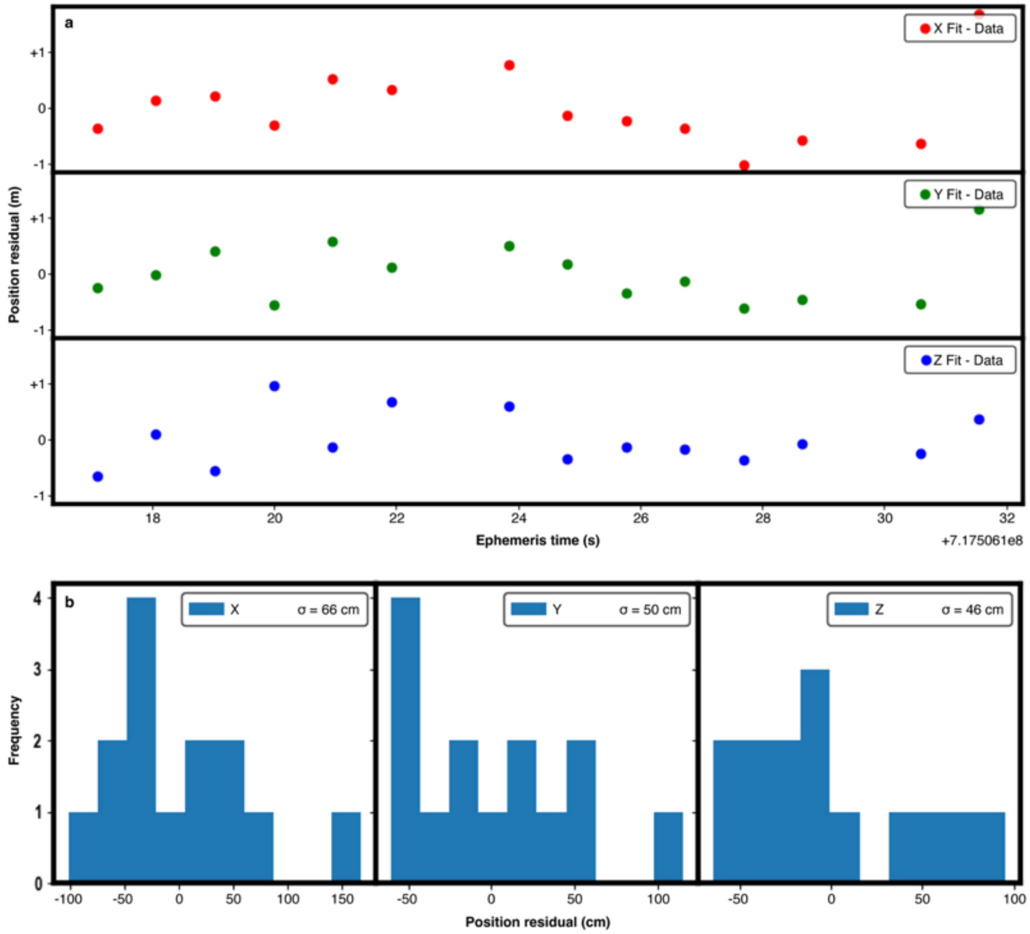
Extended Data Figure 7



Extended Data Figure 8



Extended Data Figure 9



Extended Data Figure 10